

Flowfield Measurements in the Endwall Region of a Stator Vane

M. B. Kang¹

K. A. Thole²

Mechanical Engineering Department,
Virginia Polytechnic Institute
and State University,
Blacksburg, VA 24061

A first-stage stator vane experiences high heat transfer rates, particularly near the end-wall, where strong secondary flows occur. In order to improve numerical predictions of the complex endwall flow at low-speed conditions, benchmark quality experimental data are required. This study documents the flowfield in the endwall region of a stator vane that has been scaled up by a factor of nine while matching an engine exit Reynolds number of $Re_{ex} = 1.2 \times 10^6$. Laser Doppler velocimeter (LDV) measurements of all three components of the mean and fluctuating velocities are presented for several flow planes normal to the turbine vane. Measurements indicate that downstream of the minimum static pressure location on the suction surface of the vane, an attenuated suction side leg of the horseshoe vortex still exists. At this location, the peak turbulent kinetic energy coincides with the center of the passage vortex location. These flowfield measurements were also related to previously reported convective heat transfer coefficients on the end-wall showing that high Stanton numbers occur where the passage vortex brings mainstream fluid toward the vane surface. [S0889-504X(00)00803-5]

Introduction

Today's gas turbine designs have the aim of increasing turbine vane heat loads while improving the durability. To accommodate these demands, an understanding of the relevant flow mechanisms affecting the turbine vane heat transfer and aerodynamic losses is needed to insure peak performance. One region that can impact turbine vane durability is the endwall or platform area where the flow is quite complex.

As the endwall boundary layer approaches the stagnation location of the protruding airfoil, it experiences an increase in pressure causing a stronger deceleration for the higher speed fluid than the lower speed fluid in the boundary layer. The differences in the deceleration gives rise to a transverse pressure gradient along the vane causing the higher speed fluid to turn toward the endwall. Subsequently, the formation of a horseshoe vortex occurs just upstream of the turbine vane. One leg of the horseshoe vortex wraps around the pressure side of the vane. While the pressure side leg joins into what is known as the passage vortex, there is more uncertainty as to how the suction side leg develops through the passage. The suction side leg of the horseshoe vortex moves along the suction side of the vane and has the opposite sense of rotation as the passage vortex.

Although there have been a number of endwall flowfield studies, many of those studies have been for rotor blades as compared to stator vanes where stators generally have smaller turning angles and higher flow accelerations. The flowfield measurements presented in this paper are for a stator vane geometry. This work is also important because there has been a rather limited number of studies with reported turbulence measurements and because this study relates the measured surface heat transfer to the measured flowfields.

Past Studies

Throughout the literature there have been a number of proposed endwall flowfield models. Sieverding [1] presents a summary of these models including one of the first given by Langston et al.

¹Present address: Boeing Defense & Space Group, 6633 Canoga Ave., P.O. Box 7922, Canoga Park, CA 91309-7922.

²Present address: Mechanical Engineering Department, Virginia Polytechnic Institute and State University, Blacksburg, VA 24061.

Contributed by the International Gas Turbine Institute and presented at the 44th International Gas Turbine and Aeroengine Congress and Exhibition, Indianapolis, Indiana, June 7–10, 1999. Manuscript received by the International Gas Turbine Institute February 1999. Paper No. 99-GT-188. Review Chair: D. C. Wisler.

[2]. Sharma and Butler [3], Goldstein and Spores [4], and Wang et al. [5] have proposed other models. All of these studies include a horseshoe vortex at the leading edge-endwall intersection with pressure-side and suction-side legs. The differences between these models have been on the role of the leading edge vortex that wraps around the suction side. While Sharma and Butler [3] suggest that the suction side leg is entwined with the passage vortex, Goldstein and Spores [4] show a distinct vortex rising along the span of the turbine blade above the passage vortex. Wang et al. [5] indicated a number of additional vortices occurred in the end-wall region for their low Reynolds number study. Gregory-Smith and Cleak [6] indicated the existence of the suction side leg of the horseshoe vortex only at a position close to the suction-endwall corner very near to the leading edge of their rotor blade. Gregory-Smith and Cleak [6] had a relatively large aspect ratio of 2.1 for their rotor blade study. The fact that they reported the suction side vortex only near the vane-endwall corner may have been influenced, however, by the fact that they had a laminar separation bubble on the suction side of the rotor. Alternatively, Moore et al. [7], who had an aspect ratio of 1, reported fluid from the suction side leg of the horseshoe vortex had convected to the outside of the passage vortex away from the suction surface. Moore et al. [7], however, had placed a boundary layer trip on the blade itself, which may have also influenced the endwall flow.

While several investigators have reported some turbulence measurements, for example Bailey [8] and Moore et al. [7], the majority of these measurements have reported measurements at a location downstream of the passage exit. The most detailed turbulence field measurements inside the passage have been those reported by Gregory-Smith et al. [9] for a rotor blade endwall region. Gregory-Smith et al. [9] reported turbulence levels as high as 29 percent in the vortex core where these high turbulence levels were associated with large aerodynamic losses. In a later study, Gregory-Smith et al. [9] used a grid having an inlet turbulence level of 5 percent to remove the boundary layer separation on the blade. In this study they reported high turbulent Reynolds stresses in the vortex.

Boyle and Russell [10] performed surface heat transfer experiments over a large Reynolds number range for a stator vane geometry. At low Reynolds numbers, they found that Stanton number contours closely followed the inviscid streamlines from the pressure side to the suction side of the airfoil. At higher Reynolds numbers the surface heat transfer correlated closely with the free-stream velocity and thereby appeared more similar to the static

pressure contours. In relating information from the flow visualization to the heat transfer data, Gaugler and Russell [11] combined two studies, their own and that of York et al. [12], for a large-scale turbine vane in which they found that the peak Stanton number coincided with the region having the most intense vortex action.

Based on past studies, there is a clear need to investigate further the heat transfer characteristics of the endwall of a modern day stator vane. Although there has been a link between flowfield visualization and surface heat transfer measurements, a link between measured secondary flows and measured heat transfer is still needed. In addition, benchmark quality flowfield data, including both mean and turbulent velocities, are still needed for comparisons with computational predictions for a vane.

Experimental Design and Measurements

A stator vane, scaled up by a factor of nine, was placed in a wind tunnel facility for this study. The experiment was designed to have a large scaling factor to allow for good measurement resolution in an existing wind tunnel. The construction and the development of the scaled-up stator turbine vane and the test section have been previously documented by Kang et al. [13]. The wind tunnel used in this study is recirculating with a corner test section, shown in Fig. 1(a). This test section contains a scaled-up central turbine vane with two adjacent vanes. The outside adjacent vane was constructed by attaching a leading edge to a plexiglass sidewall allowing for optical access. The placement of this flexible wall exactly matches that surface of an adjacent vane. At the point where an adjacent vane geometry stops, the flexible wall was positioned such that the central vane matched the two-dimensional, inviscid pressure distribution computationally predicted for periodic vanes at low-speed conditions. Pressure measurements on the central vane were made to insure that the flexible wall and stagnation point were positioned correctly. For

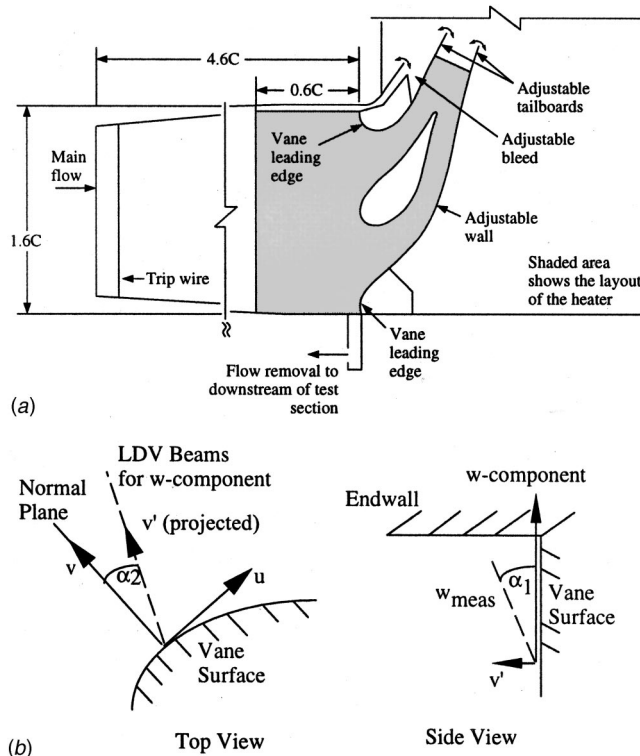


Fig. 1 (a) Top view of the corner test section; (b) velocity correction scheme for the w component

Table 1 Geometric and flow conditions for the stator vane

Scale factor	9
Scaled-up true chord length	59.4 cm
Pitch / true chord	0.77
Span / true chord	0.93
Re_{ex}	1.2×10^6
Inlet and exit angles	0° and 78°
Approach length / true chord	4.6

Table 2 Boundary layer parameters one chord upstream

δ_{99} (cm)	5.0
δ^* (cm)	1.06
θ (mm)	7.1
H	1.50
Re_θ	3340
U_∞ (m/s)	7.33
Re_{ex}	1.2×10^6

the data presented in this paper, flowfield measurements were taken at locations only upstream of where an actual adjacent vane would geometrically end for the passage.

The upstream side wall boundary layers were removed by adjustable bleeds while tailboards on the outer vanes insured that periodic flow occurred in both passages around the central airfoil (Radomsky and Thole, [14]). The flow was prevented in going from the pressure to the suction sides under the vane by applying a sealant at the base of the vane. A description of the turbine vane itself is given by Table 1.

Inlet boundary layer measurements were made one chord upstream of the stator vane test section on the top and bottom endwalls (Kang et al. [13]). The inlet boundary layer parameters are listed in Table 2. Note that the incident turbulence level upstream of the vane was 0.6 percent. The ratio of boundary layer thickness-to-span is $\delta_{99}/S = 0.09$ for $Re_{ex} = 1.2 \times 10^6$.

Flowfield Measurements

The two-component back-scatter fiber optic LDV system used in this study consisted of a 5 W laser and a TSI model 9201 Colorburst beam separator. Velocity data were processed using a TSI model IFA 755 Digital Burst Correlator controlled using the TSI FIND software. Two different focusing lenses were used for these measurements. The 350 mm focusing lens without a beam expander was used to make measurements of the streamwise (u) and pitchwise (v) components through the top endwall. The spanwise component (w) was measured from the side using the 750 mm focusing lens with a beam expander, as indicated in Fig. 1(b). The probe volume length and diameter for the 350 mm lens were 1.3 mm and $90 \mu\text{m}$ whereas the probe volume length and diameter for the 750 mm lens with the beam expander were 0.85 mm and $46 \mu\text{m}$. For each component of velocity, 10,000 data points were measured to compute mean and turbulence quantities. The LDV data were corrected for biasing using residence time weighting.

To allow measurements to be made close to the endwall–vane surface, the LDV fiber optic probe needed to be slightly tilted off of the vane spanwise axis by an angle of α_1 . For the pressure side planes, the probe needed to be tilted slightly off the axis normal to the vane surface by an angle of α_2 to insure that measurements along the pressure side of the vane were not blocked by the inside adjacent vane. Because of these tilts, the measured spanwise velocity component (w_{meas}) needed to be corrected to get the true spanwise velocity component (w). This correction was possible since the true streamwise and pitchwise velocity components

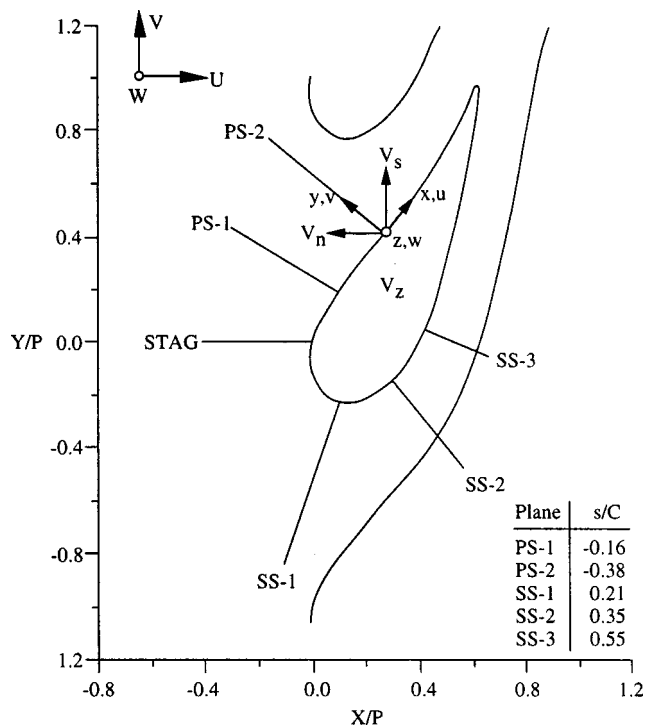


Fig. 2 Locations of the flowfield measurement planes

(with respect to the vane surface) were also measured. The correction scheme that was applied is illustrated in Fig. 1(b) and given by the following relation:

$$w = [w_{\text{meas}} \cos \alpha_1 - v' \sin \alpha_1] \quad (1)$$

where v' is the velocity component projected normal to the measurement plane calculated from the relation,

$$v' = v \cos \alpha_2 + u \sin \alpha_2 \quad (2)$$

The spanwise tilt for all of the planes was $\alpha_1 = 4.8$ deg. The normal axis tilt was $\alpha_2 = 30$ deg and 17 deg for the PS-1 and PS-2 planes, respectively. There was no normal axis tilt for the suction side planes. The largest corrections occurred at the vane midspan due to the high streamwise velocity component, u . Near the wall the correction was much smaller.

Flowfields were measured for two pressure side planes (PS-1 and PS-2) and three suction side planes (SS-1, SS-2, and SS-3) where those planes were orthogonal to the vane surface, as shown in Fig. 2. Note that Kang et al. [13] previously presented flowfield results for the stagnation plane (STAG). The measured local velocity components (u , v , and w) are also shown in Fig. 2. These velocities were then transformed into the streamwise, normal, and spanwise components (V_s , V_n , and V_z) as discussed later in the text.

Endwall Heat Transfer Measurements

Previously reported heat transfer results will be used in this study to relate the secondary flows to the surface heat transfer. A full description of the heat transfer experiments and data is given by Kang et al. [13] and will be briefly described here. The heat transfer results were obtained with a constant heat flux plate that was placed on the bottom endwall surrounding the Styrofoam stator vane. A calibrated infrared camera was used to collect the surface temperature information from the constant heat flux plate on the bottom endwall. The input heat flux was corrected for radiation losses, which amounted to between 4–23 percent of the input power, and conduction losses, which amounted to 1.7–3.5 percent of the input power. No correction was necessary regarding

Table 3 Uncertainty estimates

Value	Uncertainties
St	4.5% for $St = 3 \times 10^{-3}$ ($\Delta T = 5^\circ\text{C}$)
V_s	1% near vane-endwall
V_n	7.5% near vane-endwall
V_z	1.5% near vane-endwall
k	2.4% near vane-endwall
SKE	3.5% near vane-endwall
ψ	1.5% near vane-endwall
ϕ	1% near vane-endwall

heat losses from conduction to the turbine vane itself because the vane was constructed using Styrofoam. Using the measured temperatures and the remaining convective heat flux, the heat transfer coefficients were computed.

Uncertainty Estimates

Uncertainties were calculated based on a 95 percent confidence interval. The partial derivative and sequential perturbation methods, described by Moffat [16], were used to estimate the uncertainties of the measured values. The estimates of uncertainties on each of the values presented in this paper are given in Table 3. Note that the uncertainty estimates were made for the near-endwall region where the highest uncertainties arise. The uncertainty in the Stanton number was quoted for the lowest temperature difference measured which dominated the total uncertainty. The uncertainty for the normal velocity (V_n) was significantly higher than the other velocity components and primarily arose from the uncertainty in the flow angle at the midspan location. For V_n , both u and v velocity components contributed with neither dominating. In comparison for V_s , the term $u \cos \psi_{ms}$ is quite large with the u component dominating. While for V_s the uncertainty was dictated by the uncertainty in the u component, the uncertainty for V_n was dictated by the uncertainty in ψ_{ms} .

Flowfield Analysis

The primary interest of this study was to discern the horseshoe vortex legs and the passage vortex convecting through the turbine vane passage. The velocity vectors of these vortices, which will be referred to as the secondary flow vectors, were determined by transforming the measured local velocities (u , v , and w in Fig. 2) into the mean flow direction based on that occurring at the midspan (V_s , V_n , and V_z). For this transformation the inviscid turning angle was calculated based on the measured velocities at the vane midspan (u_{ms} and v_{ms}) from the following relation:

$$\psi_{ms} = \tan^{-1}(v_{ms}/u_{ms}) \quad (3)$$

The local transformed velocities were calculated using the following:

$$V_s = u \cos \psi_{ms} + v \sin \psi_{ms} \quad (4)$$

$$V_n = -u \sin \psi_{ms} + v \cos \psi_{ms} \quad (5)$$

$$V_z = w \quad (6)$$

The secondary flow vectors are plotted using the components normal to the mean flow direction (V_n , V_z).

In addition to the transformed velocities, contours of the secondary kinetic energy, turbulent kinetic energy, pitch and yaw flow angles are also presented. The normalized secondary kinetic energy is calculated from the following relation:

$$\text{SKE} = (V_n^2 + V_z^2) / \int_0^S \int_0^S U_{in}^2 dz \quad (7)$$

Note that the denominator for the SKE is the inlet kinetic energy calculated across the entire span including the endwall boundary layers. The turbulent kinetic energy (k) and the pitch (ϕ) and yaw (ψ) flow angles were calculated using the relations given in the nomenclature.

Results

The results presented in this paper are for several planes orthogonal to the scaled-up turbine vane on the suction and pressure sides. Prior to making measurements of the flowfield along the endwall pressure and suction surfaces, measurements were made at the vane midspan to compare with those predicted. These measurements were made to insure that the flowrates in each of the two passages were matched and good inlet conditions were achieved. The prediction was made using the two-dimensional, inviscid solver RAMPANT [15]. The computational domain included one passage with periodic boundary conditions.

Figure 3(a) shows a comparison of the measured static pressure distribution and the predicted static pressure distribution from the two-dimensional, inviscid, low-speed calculation. Figure 3(b) compares the velocity components for the inside and outside vane passages as compared with that predicted by RAMPANT for a measurement location at the vane geometric stagnation location. These measurements indicate good periodic flow conditions on the inside and outside passages around the central turbine vane.

Figures 4(a) and 4(b) compare the measured and predicted streamwise velocities and flow angles for each of the flow planes measured at the vane midspan. Note that $y/P=0$ is always measured normal to and outward from the vane surface. Again, the measured values are compared with that predicted using

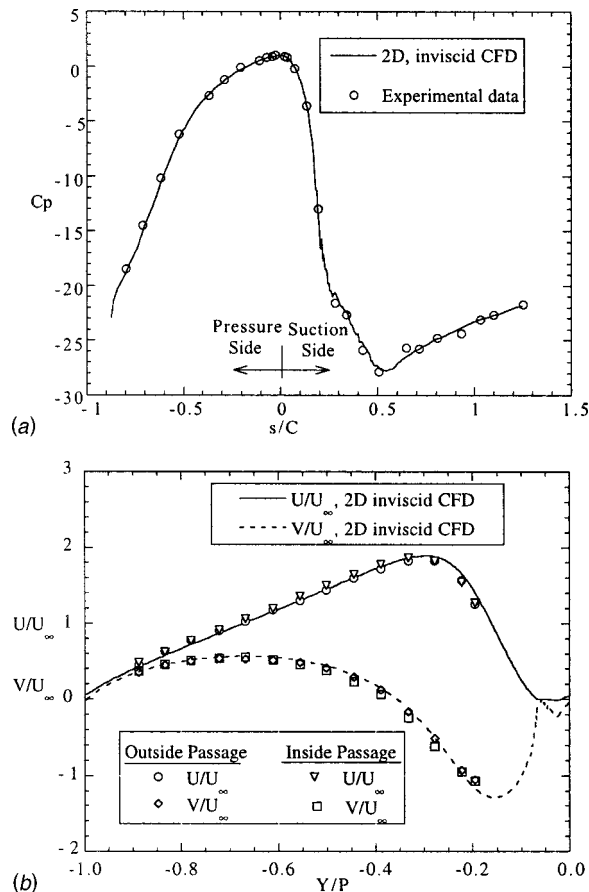


Fig. 3 (a) Static pressure distribution for vane geometry; (b) velocity measurements for inside and outside passages around the central vane compared with CFD

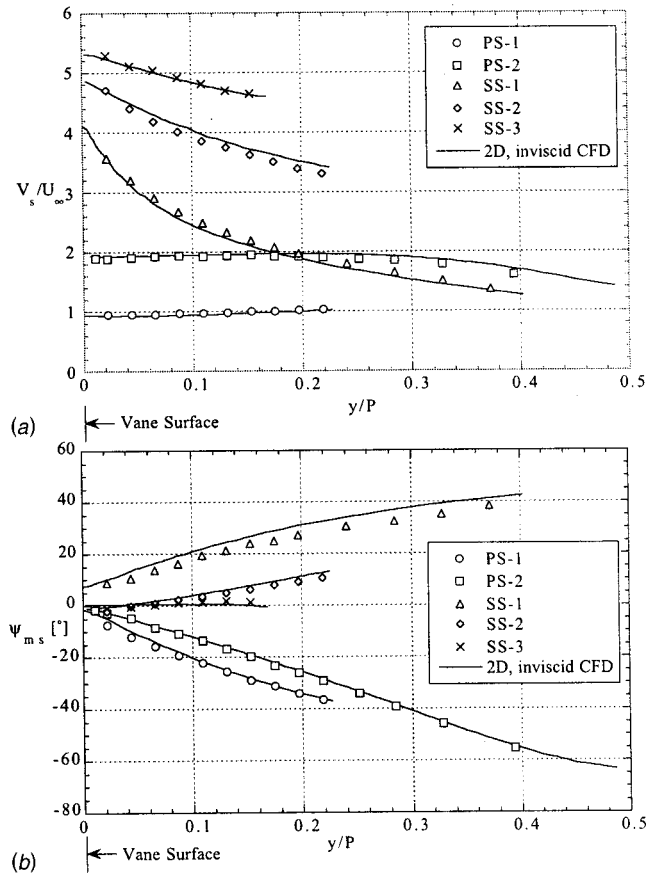


Fig. 4 Comparison of measured and predicted: (a) V_s/U_∞ , and (b) Ψ_{ms} , at the vane midspan

RAMPANT. These results indicate good agreement between that predicted and measured. Across the pressure side planes there is a fairly uniform streamwise velocity while, as expected, there is a large variation across the suction side planes. The flow angles show large turning for the first locations on the pressure and suction sides. Farther downstream, the flow angles are such that the flow is parallel with the surface on the suction side.

Pressure Side Flowfield. Figure 5(a) shows contours of the mean streamwise velocity (V_s) superimposed on the secondary flow vectors for the PS-1 plane for an exit Reynolds number of $Re_{ex}=1.2 \times 10^6$. Note that the velocity components are normalized by the upstream inlet velocity and the vector scale above the plot shows a unit vector. The location $y/P=0$ is where the surface of the pressure side of the vane is located. At this location, only the passage vortex is detected, which means that the pressure side leg of the horseshoe vortex has already merged with the passage vortex. As expected from past studies, the passage vortex is turning in the clockwise direction. The center of the vortex is located off the vane at $y/P=0.125$ at a spanwise position of $z/S=0.04$, which is slightly below the edge of the boundary layer. It is clear that the vortex has skewed the streamwise velocity contours such that high-speed fluid has been brought down close to the endwall at the location where there is a downward vortex motion. Previously Kang et al. [13] presented surface streakline visualization on the endwall showing that the separation line for PS-1 occurred at $y/P=0.15$, which coincides with the slight positive w component measured on the outside of the vortex. Mainstream fluid is being pulled down by the vortex toward the endwall at a spanwise position as high as $z/S \sim 0.22$. Contours of the secondary kinetic energy (Eq. (7)) normalized by the inlet kinetic energy are shown

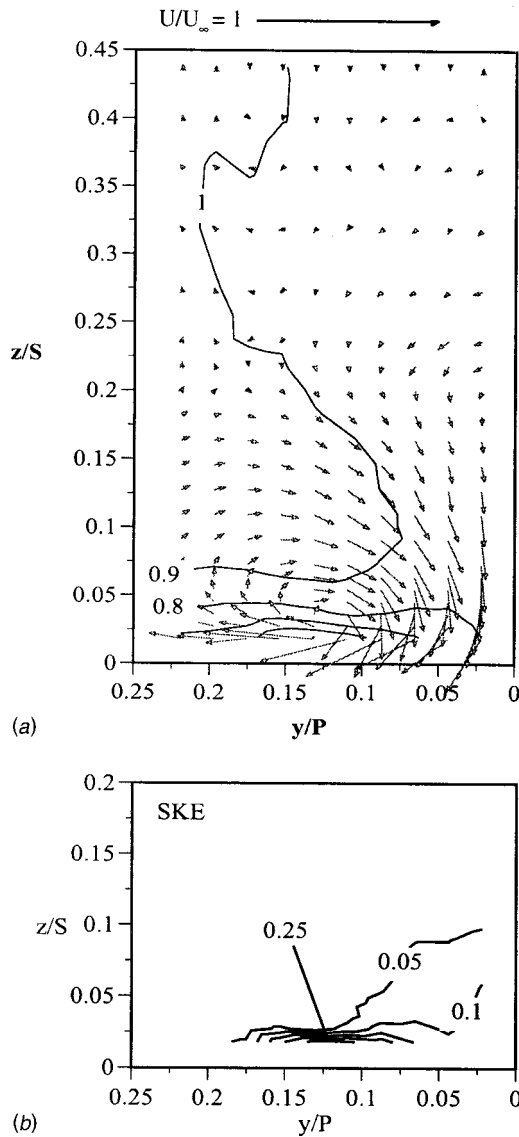


Fig. 5 Measurements of: (a) V_s/U_∞ and secondary velocity vectors, and (b) secondary kinetic energy contours for PS-1

in Fig. 5(b). Contours of the secondary kinetic energy show that the peak value occurs near the endwall surface at a pitch location corresponding to the center of the vortex.

Figure 6(a-d) presents the turbulent velocity fluctuations at PS-1 of all three velocity components along with the combined fluctuations in terms of a turbulent kinetic energy. The peak streamwise velocity fluctuation (u_{rms}) is significantly lower than the other fluctuating velocities with the peak for the spanwise velocity fluctuation (w_{rms}) being the highest. These trends in the relative levels of the streamwise and spanwise velocity fluctuations are the same for all of the other flow planes that have been measured, and are consistent with the measurements presented by Gregory-Smith and Cleak [6]. The peak rms levels for PS-1 all occur at a pitch position that corresponds to the center of the vortex but are at a spanwise position nearer to the endwall at $z/S=0.03$. The peak in turbulent kinetic energy level also occurs at the same pitch position, but slightly closer to the endwall than the center of the vortex. In converting the turbulent kinetic energy to a turbulence intensity, the peak corresponds to a turbulence intensity of 26 percent based on the inlet velocity. The k/U_∞^2 contours are somewhat asymmetric in that closest to the pressure

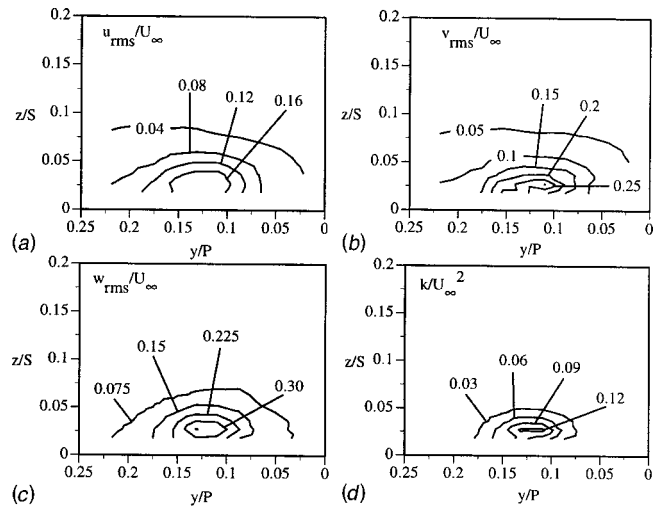


Fig. 6 Normalized contours of measured: (a) u_{rms}/U_∞ , (b) v_{rms}/U_∞ , (c) w_{rms}/U_∞ , and (d) k/U_∞^2 for the PS-1 plane

side vane surface the contours are wrapped under, while away from the vane surface the contours indicate little spanwise gradient.

The yaw angle contours shown in Fig. 7(a) for PS-1 are levels where the midspan value have been subtracted off for that given pitch location ($\psi - \psi_{ms}$). The ψ_{ms} values used for each given pitch location were taken from Fig. 4(b). The pitch flow angle (ϕ) at the midspan location was zero. The yaw contour levels for PS-1 are large positive values near the endwall surface, indicating that close to the endwall the boundary layer fluid is turning much less than at the midspan location. The lower velocity boundary layer fluid does not react to the upcoming vane surface and has a tendency to continue flowing in the same direction as at the inlet. Above the vortex center, which is located near the edge of the boundary layer, the contour levels are negative, indicating the flow is turning slightly more than at the midspan location. These negative values occur because of the streamwise vorticity that the flow experiences as it progresses through the passage. Clearly, the flow in the endwall region is quite skewed. The pitch flow angles, shown in Fig. 7(b), indicate very strong negative values near the endwall-vane corner on the downward side of the vortex leg. The magnitude of the pitch angles on the upward side of the vortex leg indicate that there is only a slight upward curling of the vortex. The cross-pitch pressure gradient drives the flow along the endwall from the pressure surface to the suction surface.

Figure 8(a) shows the secondary velocity vectors superimposed with the streamwise velocity contours for PS-2. The center of the vortex is located at approximately the same position off the vane and endwall as it was for PS-1 at $y/P=0.125$ and $z/S=0.04$. The

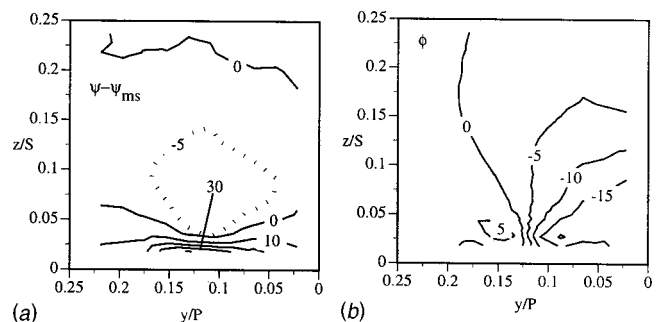


Fig. 7 Contours of measured: (a) yaw ($\Psi - \Psi_{ms}$) and (b) pitch (ϕ) angles for the PS-1 plane

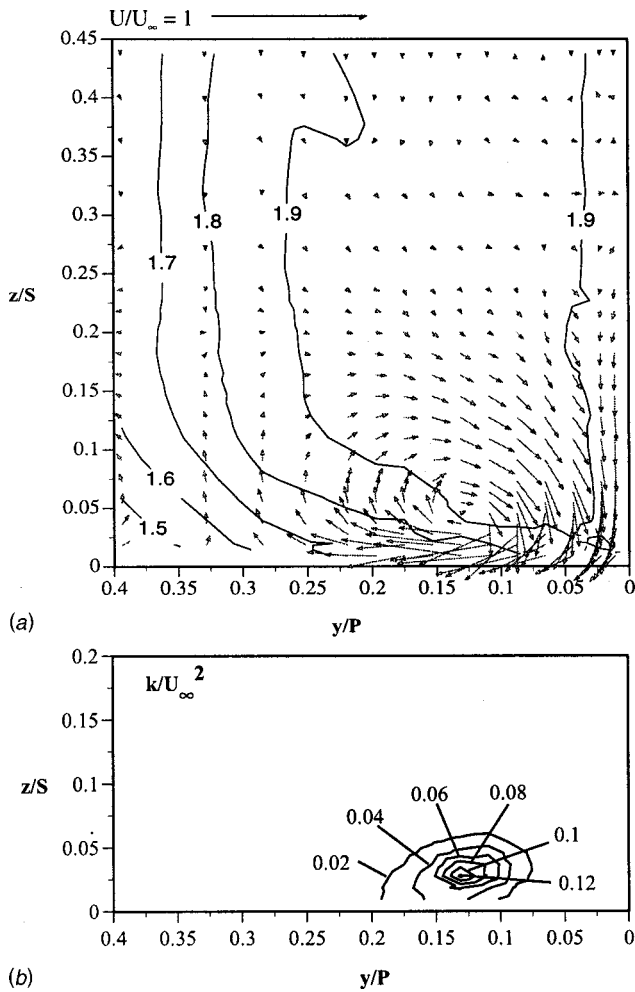


Fig. 8 Measurements of: (a) V_s/U_∞ contours and secondary velocity vectors, and (b) turbulent kinetic energy contours for PS-2

size of the vortex, however, at this location is much larger. Mainstream fluid is being pulled down along the pressure surface toward the endwall starting at a spanwise position of $z/S=0.275$, which is higher than occurred for PS-1. At this location the flow has accelerated such that the streamwise velocity component is as much as 1.9 times faster than the inlet velocity. It is clear that again the vortex has caused some skewing of the streamwise velocity profiles near the endwall at $z/S=0.05$. The turbulent kinetic energy contours for PS-2, given in Fig. 8(b), are quite similar to those for PS-1 with the only difference being a slightly larger peak region for PS-1. The peak level corresponds to the same pitch position ($y/P=0.12$) as the center of the vortex, but slightly closer to the endwall ($z/S=0.03$ for k/U_∞^2 and $z/S=0.05$ for the center of the vortex).

Suction Side Flowfield. Three planes normal to the vane were measured along the suction side of the vane. Figure 9(a) shows the secondary velocity vectors superimposed on the streamwise velocity contours for SS-1. Note that $y/P=0$ now represents the suction surface of the vane. The secondary velocity vectors show both the suction side leg of the horseshoe vortex and the passage vortex from the neighboring vane with the two vortices having opposite rotation directions. The suction leg of the horseshoe vortex is located very close to the vane surface with the center being at $y/P=0.05$. At this location, the mainstream flow has already been highly accelerated. The streamwise velocity contours near the endwall have been skewed due to the passage vor-

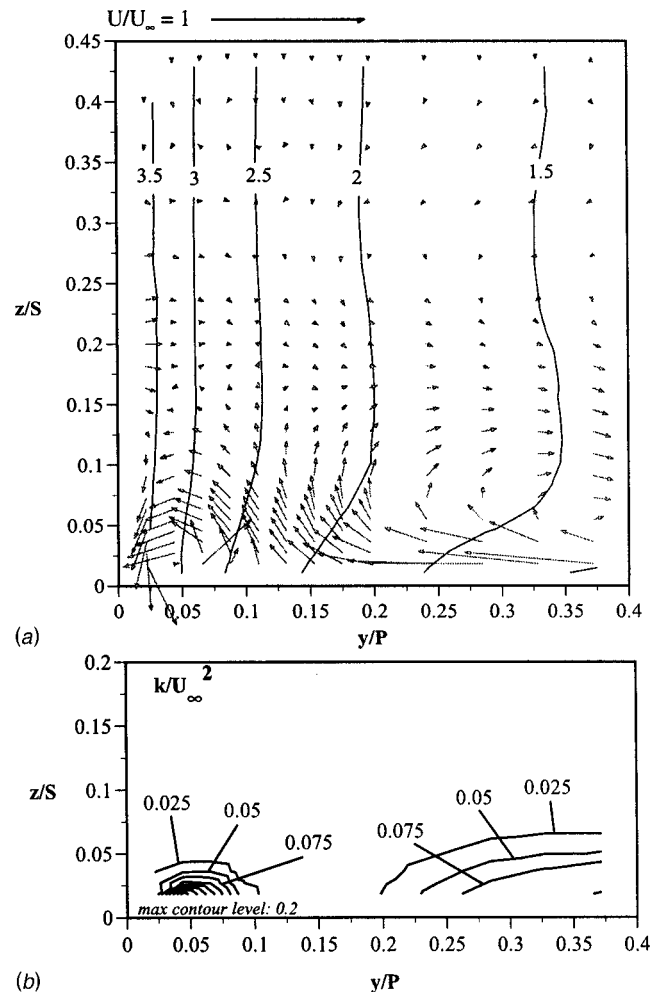


Fig. 9 Measurements of: (a) V_s/U_∞ contours and secondary velocity vectors, and (b) turbulent kinetic energy contours for SS-1

tex. Close to the vane—endwall corner, the streamwise velocity contours show no variation, indicating that the endwall boundary layer is very thin. The suction side leg of the vortex has only a slight effect on the streamwise velocity component near the vane—endwall corner.

The turbulent kinetic energy contours for SS-1, shown in Fig. 9(b), indicate two distinct contour regions for the suction side leg of the horseshoe vortex and the passage vortex. The primary difference in the turbulent kinetic energy levels are that the suction side leg of the horseshoe vortex has higher levels as compared with the passage vortex. The suction side leg of the horseshoe vortex covers a much smaller region of the endwall relative to the passage vortex. The region between the two contour levels has very low turbulence levels. The turbulent kinetic energy levels of the passage vortex shown for SS-1 are very similar to the levels that occurred for PS-1.

The secondary flow vectors and streamwise velocity contours for SS-2 are shown in Fig. 10(a) while the turbulent kinetic energy contours are given in Fig. 10(b). The measurement plane SS-2 is at a surface distance from the stagnation position along the suction surface at $s/C=0.4$, which is still in the acceleration region and just slightly before the minimum static pressure on the vane surface. At this location the suction side leg of the vortex still exists, with the size of the suction leg vortex being much smaller than the passage vortex. The passage vortex has moved significantly closer to the vane surface as compared with SS-1. The streamwise velocity contours show that at this location the

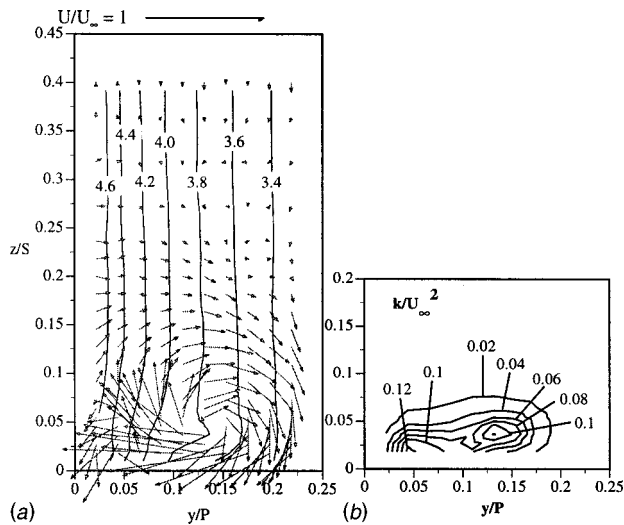


Fig. 10 Measurements of: (a) V_s/U_∞ contours and secondary velocity vectors, and (b) turbulent kinetic energy contours for SS-2

velocity has accelerated to between three and four times the inlet velocity.

The turbulent kinetic energy contours for SS-2 in Fig. 10(b) still show two distinct peak regions from the two vortices but with some overlapping. The one difference between these two high turbulence regions is that the peak turbulence region for the passage vortex is somewhat farther off the endwall than for the suction side vortex. The turbulent kinetic energy contours also show similar contour levels for the two vortex regions with the peaks occurring at the vortex centers. The passage vortex is slightly higher off the endwall than the suction side vortex.

The measurement plane SS-3 is at a surface distance from the stagnation location of $s/C=0.56$, which is approximately the position where the minimum static pressure on the vane occurs. At this location, Fig. 11(a) shows that the passage vortex is quite strong and affecting the mean streamwise velocity components. A suction side leg of the horseshoe vortex very near to the vane surface is still evident, but is very small for the SS-3 plane. The center of the passage vortex is located at a pitch distance even closer to the vane surface at $y/P=0.12$ as compared with the SS-2 where the passage vortex center is located at $y/P=0.14$. The center of the passage vortex is also located slightly higher in the span direction for SS-3 as compared with SS-2. It is clear from the measurements shown in SS-3 that the suction side leg of the horseshoe vortex is being attenuated by the passage vortex at the vane-endwall junction. At this location, the measurements do not agree with the model proposed by Goldstein and Spores [4], who suggested that the suction leg remains distinct rising along the span of the turbine blade above the passage vortex beginning downstream of the boundary layer separation line. The SS-3 plane, shown in Fig. 11(a), is downstream of the separation line. It should be pointed out, however, that the Goldstein and Spores results were for a rotor blade.

The peak turbulent kinetic energy level for SS-3, shown in Fig. 11(b), is much higher than any of the other flow plane locations. Another difference for this plane is that the peak turbulent kinetic energy level is at a pitch and span position that correspond to the center of the vortex. This is distinctly different from the other planes in that the peak level has typically occurred at a spanwise position just below the center of the vortex. The presence of the highly turbulent fluid farther off the endwall is due to the lift induced by the passage vortex.

Contours of the secondary kinetic energy Eq. (7), which has been normalized by the inlet kinetic energy, for SS-3 are shown in

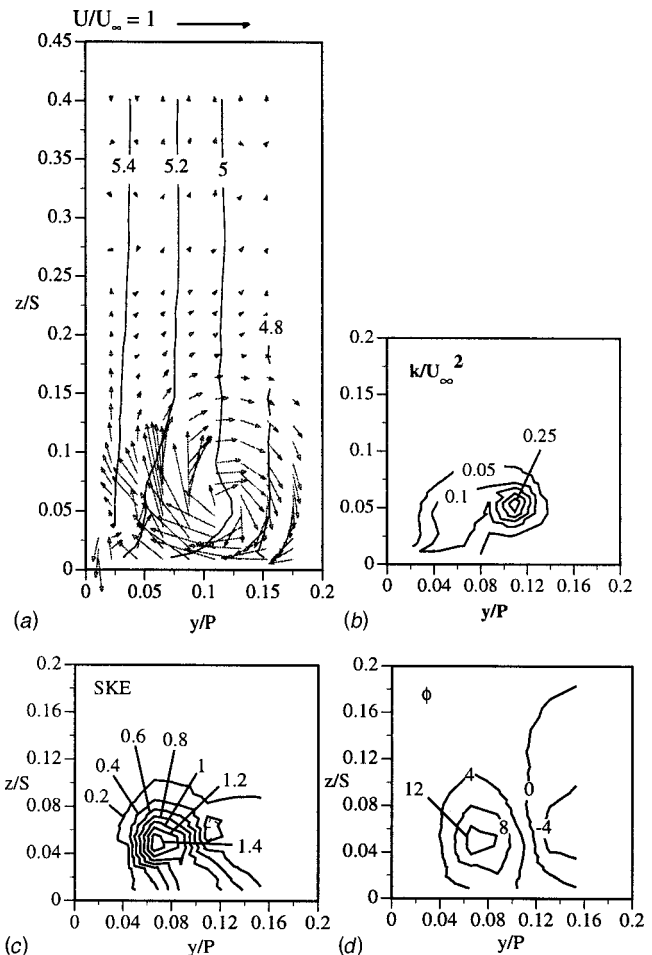


Fig. 11 Measurements of: (a) V_s/U_∞ contours and secondary velocity vectors; (b) turbulent kinetic energy contours for SS-3. Contours of measured: (c) secondary kinetic energy, and (d) pitch (ϕ) angles for the SS-3 plane.

Fig. 11(c). Compared with PS-1, the secondary kinetic energy levels are much higher. Another large difference between PS-1 and SS-3 is that for SS-3 the peak level occurs much off the endwall surface at $z/S=0.05$. The yaw angles relative to that at the midspan for SS-3 indicate much smaller values as compared with PS-1. While there are higher negative pitch values for PS-1, there are much higher positive pitch values for SS-3, shown in Fig. 11(d). The higher positive pitch values for SS-3 indicate that the passage vortex is lifting off the endwall surface. This has been previously reported through endwall visualization studies indicated by the ink climbing onto the suction surface.

Convective Heat Transfer Coefficients for Measured Flow-field Planes.

The local heat transfer coefficients on the endwall for each of the flow plane locations were obtained from the previously reported Stanton number contours by Kang et al. [13]. Note that the Stanton numbers presented by Kang et al. used the upstream inlet velocity for scaling the local heat transfer coefficients. The Stanton numbers shown in Fig. 12 for each of the flow planes are based on the local streamwise velocity (V_s) at the vane midspan. By using the local midspan streamwise velocity as the normalizing scale, the effect of the secondary flows on the surface heat transfer can be addressed. The farthest y/P location where the Stanton numbers are plotted in Fig. 12 corresponds to the last measurement location in that flow plane.

For both the stagnation region and the pressure side of the vane, the highest Stanton number values occur nearest to the vane sur-

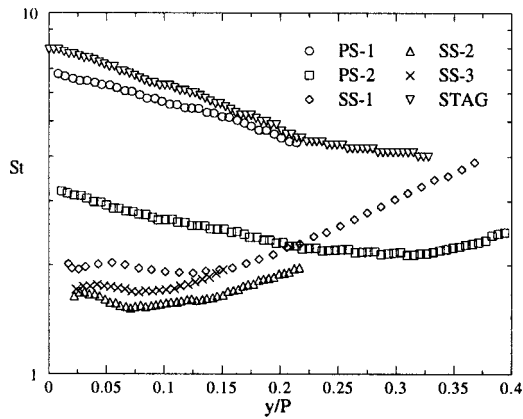


Fig. 12 Stanton number based on V_s for all the planes (based on measured heat transfer coefficients from Kang et al. [13])

face. These peak values occur where the secondary flows are bringing the high-speed mainstream fluid down toward the endwall thereby thinning the boundary layer. Where the secondary flow is turning upward, the Stanton numbers remain relatively constant. Further away from the vane surface at PS-2, the Stanton numbers again increase at $y/P=0.3$. This increase occurs due to the influence of the horseshoe vortex from the adjacent vane. Although V_s has increased for PS-2 and has been taken into account, the flow condition on the pressure side significantly decreased St for PS-2 relative to PS-1.

For the suction side, moving away from the vane there is first a slight increase in the Stanton number, between $y/P=0.03$ and 0.05 , due to the downward motion of the suction side leg vortex. This increase is then followed by a decrease, with the minimum Stanton number occurring near where the suction side leg of the horseshoe vortex and passage vortex meet. Beyond this point, where the passage vortex is turning upward, there is a rapid increase in the Stanton number. This increase is caused by the upward turning of the passage vortex. Progressing from SS-1 to SS-2, there is a decrease in the overall Stanton number levels. The Stanton numbers for SS-2 and SS-3 are the same close to the vane with only slight differences further away from the vane. Surface heat transfer measurements on the vane midspan indicate that the transition to turbulent flow occurs near the SS-3 vane position (Radomsky and Thole, [14]).

Conclusions

This paper has presented detailed mean and turbulent statistics for the endwall region of a stator vane geometry. The flowfield measurements along the pressure side of the vane indicated that at a position fairly close to the flow stagnation location, only the passage vortex was present, and any remnants of the pressure side leg of the horseshoe vortex were no longer evident. The rms levels of the turbulent fluctuations indicated that the spanwise velocity fluctuations were typically higher than either the streamwise or cross-span fluctuations. The peak turbulent kinetic energy coincided with the same pitch location as the center of the passage vortex region, but at a span position slightly closer to the vane endwall for most of the flow planes measured. The only flow plane where this differed was at the minimum static pressure location on the suction side of the vane. At this location the peak turbulent kinetic energy coincided with the center of the vortex. For this flow plane, high positive pitch values were deduced indicating a lift from the endwall.

The suction side flow planes showed evidence of both the passage and suction side leg of the horseshoe vortex at the farthest downstream position measured, which, again, coincided with the minimum static pressure location along the vane midspan. The

suction side vortex at this location was, however, being attenuated by the passage vortex, which filled almost the entire passage.

The heat transfer measurements showed high Stanton numbers occurred where the mainstream fluid was being brought down to the endwall surface due to the downward leg of the vortices. This happened for both the remnants of the leading edge vortex as well as the passage vortex. As the passage vortex turned upward, there was a decrease in the Stanton numbers across the passage.

Acknowledgments

The authors would like to thank William Kvasnak and Fred Soechting at Pratt & Whitney, W. Palm Beach, Florida, for their support of this work. Thanks for partial support from the DOE-Advanced Gas Turbine Systems Research Program and to Dan Fant for being the contract monitor.

Nomenclature

C	= true chord of stator vane
C_p	= pressure coefficient = $1 - (P_{0,in} - P_s)/(0.5\rho U_{in}^2)$
H	= shape factor = δ^*/θ
k	= turbulent kinetic energy = $1/2(u_{rms}^2 + v_{rms}^2 + w_{rms}^2)$
P_0, p_s	= total inlet and local static pressures
P	= vane pitch
Re_{ex}	= Reynolds number, defined as $Re_{ex} = CU_{ex}/\nu$
Re_θ	= Reynolds number, defined as $Re_\theta = U_{in}\theta/\nu$
s	= vane surface distance from flow stagnation
S	= span of stator vane
SKE	= secondary kinetic energy
St	= Stanton number, defined as $St = h/\rho C_p V_s$
U, u	= reference and local mean velocities; see Fig. 2
v'	= projected velocity component, see Fig. 1(b)
V, v	= reference and local mean velocities; see Fig. 2
V_n	= transformed mean normal velocity
V_s	= transformed mean streamwise velocity
V_z	= transformed mean spanwise velocity
W, w	= reference and local mean spanwise velocities; see Fig. 2
X, x	= reference and local streamwise coordinate; see Fig. 2
Y, y	= reference and local normal coordinate; see Fig. 2
Z, z	= reference and local spanwise coordinate; see Fig. 2
α	= LDV tilt angle; see Fig. 1(b)
δ_{99}	= boundary layer thickness
δ^*	= displacement thickness
θ	= momentum thickness
ϕ	= pitch angle = $\tan^{-1}(w/u)$
ρ	= density
ν	= viscosity
ψ	= yaw angle = $\tan^{-1}(v/u)$

Subscripts

1, 2	= spanwise and normal tilt angles for LDV
avg	= average
in, ex	= inlet and exit
meas	= measured values
ms	= midspan values
rms	= root mean square

References

- [1] Sieverding, C. H., 1985, "Recent Progress in the Understanding of Basic Aspects of Secondary Flows in Turbine Blade Passages," ASME J. Eng. Gas Turbines Power, **107**, pp. 248–257.
- [2] Langston, L. S., Nice, M. L., and Hooper, R. M., 1977, "Three-Dimensional Flow Within a Turbine Cascade Passage," ASME J. Eng. Power, **99**, pp. 21–28.
- [3] Sharma, O. P., and Butler, T. L., 1987, "Predictions of Endwall Losses and Secondary Flows in Axial Flow Turbine Cascades," ASME J. Turbomach., **109**, pp. 229–236.

- [4] Goldstein, R. J., and Spores, R. A., 1988, "Turbulent Transport on the Endwall in the Region Between Adjacent Turbine Blades," *ASME J. Heat Transfer*, **110**, pp. 862–869.
- [5] Wang, H. P., Olson, S. J., Goldstein, R. J., and Eckert, E. R. G., 1997, "Flow Visualization in a Linear Turbine Cascade of High Performance Turbine Blades," *ASME J. Turbomach.*, **119**, pp. 1–8.
- [6] Gregory-Smith, D. G., and Cleak, J. G. E., 1992, "Secondary Flow Measurements in a Turbine Cascade With High Inlet Turbulence," *ASME J. Turbomach.*, **110**, pp. 1–8.
- [7] Moore, J., Schaffer, D. M., and Moore, J. G., 1987, "Reynolds Stresses and Dissipation Mechanisms Downstream of a Turbine Cascade," *ASME J. Turbomach.*, **109**, pp. 258–267.
- [8] Bailey, D. A., 1980, "Study of Mean- and Turbulent-Velocity Fields in a Large-Scale Turbine-Vane Passage," *ASME J. Eng. Power*, **102**, pp. 88–95.
- [9] Gregory-Smith, D. G., Graves, C. P., and Walsh, J. A., 1988, "Growth of Secondary Losses and Vorticity in an Axial Turbine Cascade," *ASME J. Turbomach.*, **114**, pp. 173–183.
- [10] Boyle, R. J., and Russell, L. M., 1990, "Experimental Determination of Stator Endwall Heat Transfer," *ASME J. Turbomach.*, **112**, pp. 547–558.
- [11] Gaugler, R. E., and Russell, L. M., 1984, "Comparison of Visualized Turbine Endwall Secondary Flows and Measured Heat Transfer Patterns," *ASME J. Eng. Gas Turbines Power*, **106**, pp. 168–172.
- [12] York, R. E., Hylton, L. D., and Mihelc, M. S., 1984, "An Experimental Investigation of Endwall Heat Transfer and Aerodynamics in a Linear Vane Cascade," *ASME J. Turbomach.*, **106**, pp. 159–167.
- [13] Kang, M., Kohli, A., and Thole, K. A., 1999, "Heat Transfer and Flowfield Measurements in the Leading Edge Region of a Stator Vane Endwall," *ASME J. Turbomach.*, **121**, pp. 558–568.
- [14] Radomsky, R. W., and Thole, K. A., 2000, "Flowfield Measurements for a Highly Turbulent Flow Around a Stator Vane," *ASME J. Turbomach.*, **122**, pp. 255–262.
- [15] FLUENT/UNS User's Guide, Vers. 4.2, Fluent, Inc., Lebanon, NH.
- [16] Moffat, R. J., 1988, "Describing the Uncertainties in Experimental Results," *Exp. Therm. Fluid Sci.*, **1**, pp. 3–17.